Journal of
Composites Science

MDPI

Article

Preparation of Multicomponent Biocomposites and Characterization of Their Physicochemical and Mechanical Properties

Yuriy A. Anisimov [1], Duncan E. Cree [2,*] and Lee D. Wilson [1,*]

[1] Department of Chemistry, University of Saskatchewan, Saskatoon, SK S7N 5C9, Canada; iaa365@mail.usask.ca
[2] Department of Mechanical Engineering, University of Saskatchewan, Saskatoon, SK S7N 5A9, Canada
* Correspondence: duncan.cree@usask.ca (D.E.C.); lee.wilson@usask.ca (L.D.W.); Tel.: +1-306-966-3244 (D.E.C.); +1-306-966-2961 (L.D.W.)

Received: 31 December 2019; Accepted: 30 January 2020; Published: 6 February 2020

Abstract: This work focused on a mutual comparison and characterization of the physicochemical properties of three-component polymer composites. Binary polyaniline–chitosan (PANI–CHT) composites were synthesized by in situ polymerization of PANI onto CHT. Ternary composites were prepared by blending with a third component, polyvinyl alcohol (PVA). Composites with variable PANI:CHT (25:75, 50:50 and 75:25) weight ratios were prepared whilst fixing the composition of PVA. The structure and physicochemical properties of the composites were evaluated using thermal analysis (thermogravimetric analysis (TGA), differential scanning calorimetry (DSC)) and spectroscopic methods (infrared (IR), nuclear magnetic resonance (NMR)). The equilibrium and dynamic adsorption properties of composites were evaluated by solvent swelling in water, water vapour adsorption and dye adsorption isotherms. The electrical conductivity was estimated using current–voltage curves. The mechanical properties of the samples were evaluated using dynamic mechanical analysis (DMA) and correlated with the structural parameters of the composites. The adsorption and swelling properties paralleled the change in the electrical and mechanical properties of the materials. In most cases, samples with higher content of chitosan exhibit higher adsorption and mechanical properties, and lower conductivity. Acid-doped samples showed much higher adsorption, swelling, and electrical conductivity than their undoped analogues.

Keywords: polymer composite; polyaniline; chitosan; thermal analysis; spectroscopy; adsorption; electrical conductivity; mechanical properties

1. Introduction

Polyaniline (PANI) is among a series of unique polymers studied in recent decades. The growing attractiveness, such as ease of preparation, low cost, and its multitude of applications owes to its remarkable properties. PANI-based materials are widely used in catalysis, adsorption, solar cells, battery production, gas and vapour sensors, etc. [1,2]. Although PANI has been known for well over 150 years, comprehensive studies span less than 50 years [3]. The conductive properties of PANI have potential utility for fabrication of electronic devices [4,5], batteries [6,7] and sensors [8–10]. PANI can be prepared in various product morphologies [11], where it can be combined with other polymers to prepare composite materials [12]. Such composites may have tunable properties, depending on the type of components and their composition. This study reports on three-component (ternary) polyaniline-based composite materials.

PANI is insoluble in common solvents, including aqueous media across a wide range of pH [13]. It is a thermoset polymer and, therefore, infusible since it will decompose at elevated temperature

before it melts [14]. To achieve the required properties, PANI can be modified by alteration of its functional groups by various methods of functionalization, such as cross-linking [15], grafting [16] and chemical modification [17]. A key feature related to PANI is that it retains its intrinsic properties (conductivity, thermal properties, and chemical stability) even after modification. In some cases, modification of PANI upon incorporation into composites results in enhanced textural properties (pore structure and surface area) relative to its pristine form [18]. PANI-based composites find utility in sensor devices, where such materials often display enhanced detection of rapid chemical fluctuations in the environment [19]. Such PANI composites with unique properties are known upon blending with cellulose and/or chitosan biopolymers [20,21].

Chitosan (CHT) is an abundant marine biopolymer derived from the hydrolysis of chitin [22]. Alkaline hydrolysis of chitin yields chitosan [23] with variable deacetylation, where typical commercial CHT samples have deacetylation levels that range from 70% to 95% [24]. The abundant functional groups ($–NH_2$ and –OH) of CHT are amenable for modification (Figure 1) by physical and chemical means. Cross-linking is a versatile method for modification of chitosan, where the degree of cross-linking in composite materials affects the range of swelling, mechanical, and adsorption properties [25]. In the case of biopolymer composites that contain chitosan and PANI, there is limited covalent cross-linking between polyaniline and chitosan, whereas hydrogen bond formation occurs between the –OH or $–NH_2$ groups of chitosan and the imine/amine (=N– or –NH–) groups of PANI (Figure 1b).

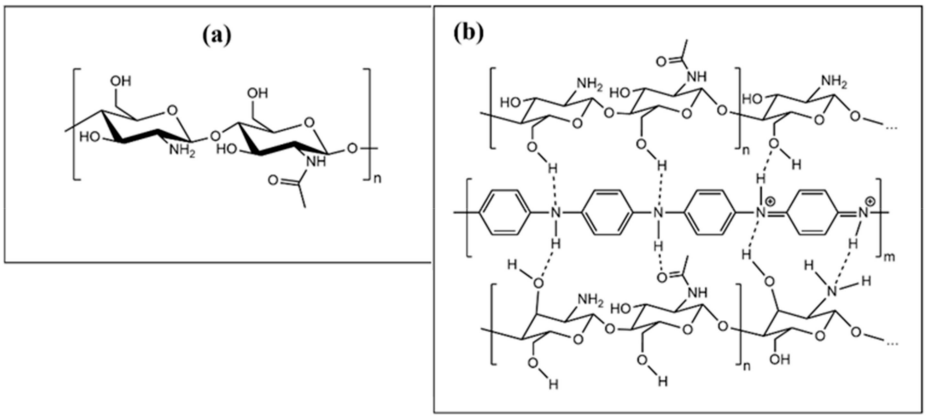

Figure 1. Schematic illustration of molecular structures of polymer fragments: (**a**) pristine chitosan with deacetylated (left) and acetylated (right) monomer units; and (**b**) CHT–PANI composite, where *n* and *m* refer to arbitrary respective chain lengths of chitosan and PANI. Panel (**b**) is based on the results reported in Reference [26].

A report on cellulose/PANI nanocomposites [21] indicated a similar structure to that shown in Figure 1b, where the extent of "hydrogen-bond mediated cross-linking" depends on the relative ratio of the precursors. In addition, the properties of such polymer composites are affected by composition such as the mechanical properties, electrical conductivity, dye adsorption and textural properties.

Although binary CHT-PANI composites possess enhanced physical properties relative to the single precursor components, their mechanical properties are not sufficiently high. These properties become modified upon physical blending with a third component, such as polyvinyl alcohol (PVA). PVA is a water-soluble synthetic polymer that possesses high hydrophilicity and plasticity suitable for production of thin films. Its water solubility is rather moderate and requires elevated temperatures to achieve higher solubility. PVA-based composite films possess enhanced mechanical properties, such as tensile strength [27]; and greater swelling (with respect to pristine PANI) due to its high propensity to absorb water. The film-forming ability of PVA allows for the formation of flexible and elastic samples; thereby widening their field of application and versatility.

Ternary PANI–CHT–PVA composites are unique materials with promising potential in the field of composite science. Although binary PANI–biopolymer composites are known [28], there are sparse

studies on ternary composite systems that contain PANI. This work details a systematic study on ternary composites (PANI–CHT–PVA) with a focus on the correlation between their adsorptive and electromechanical properties. An overall goal of this study compares the physico-chemical and physico-mechanical properties amongst composites with variable composition, and how the structure and properties are governed by their composition.

2. Materials and Methods

2.1. Materials

Aniline (density = 1.02 g/cm^3) was an ACS reagent grade (99.5%) and chitosan flakes (medium molecular weight) with a deacetylation degree 80% and a density of 0.7 g/cm^3 were obtained from Sigma-Aldrich, Oakville, ON, Canada. Chitosan is generally insoluble in pure water and sparingly soluble in acidic water media. Polyvinyl alcohol (molecular weight 78,000) was obtained from Polysciences, Inc., Warrington, PA, USA. with a density of 1.29 g/cm^3 and a degree of hydrolysis of 99%. Ammonium persulfate (APS) was an ACS reagent (98%) with a molecular weight of 228.20 g/mol that was obtained from Sigma-Aldrich, Oakville, ON, Canada. Hydrochloric acid (HCl) 36% w/w (aq) solution was obtained from Alfa Aesar, Tewksbury, MA, USA. ACS-grade (95–98%) sulfuric acid (H_2SO_4, aq) with a density of 1.84 g/cm^3 was obtained from Fischer Scientific International, Inc., Ottawa, ON, Canada. Methylene blue (MB) and the sodium salt of fluorescein (FL) sodium were of the highest available purity and obtained from Sigma-Aldrich, Oakville, ON, Canada. All solutions were prepared using highly purity Milli-Q water (resistivity 17–18 MΩ·cm).

2.2. Shorthand Notation

The shorthand notation used herein are defined below, where further details are given in Table S1 in the Supplementary Materials. In brief, the notation for the binary composites are defined according to the chitosan:PANI (CHT:PANI; w/w%) content indicated in parentheses: CHP25 (25:75), CHP50 (50:50), and CHP75 (75:25). The notation for the ternary composites differ according to the level of polyvinyl alcohol (PVA) content (w/w%), where the relative weight ratio of the aforementioned binary composite with PVA, is denoted by the following notation: CHP25-PVA, CHP50-PVA, and CHP75-PVA, where these composites contain 70% (w/w) PVA. The ternary composites that contain 50% PVA (w/w) are denoted by the following numerical index: CHP25-PVA50, CHP50-PVA50, and CHP75-PVA50.

2.3. Preparation of Polymer Composites

The synthesis of the ternary composite materials involved two steps: (1) copolymerization of aniline with the biopolymer support yielded a binary composite, and (2) preparation of the PVA blend gave a ternary composite material. The ratio of biopolymer/PANI varied from 25 to 75 wt.% biopolymer. The ratio PVA/binary material was constant and equal to 70% PVA by weight. In some cases (swelling and electrical conductivity—see Sections 3.4 and 3.7, respectively), the content of PVA was reduced to 50 wt.%.

A similar procedure for preparation of the samples was adapted from a known method [9,29]. An appropriate amount of chitosan, dissolved in 1 M HCl (100 mL), was placed in a sonicator bath for 1 h. After the system was cooled to 0 °C (ice bath), aniline was added drop-wise using a syringe. Then, the APS acidic solution (100 mL, 1M HCl) was added dropwise (0.8:1 molar ratio of APS:aniline) via a burette over a 30 min period (caution: heat evolution). The solution gradually turned to dark blue. After adding APS, the solution was stirred for 1 h. Then, the reactive solution was neutralized by NaOH and filtered. The precipitated residue was washed with water and oven-dried at 60 °C overnight. The resulting binary composite was washed again (to remove residual APS and NaOH), and then dried for 24 h. The greenish-blue colour samples were ball-milled to 32 μm mesh. PVA solutions were prepared by adding dry PVA in hot water (ca. 90 °C) in small portions every 10 min until the PVA content of 8 wt.% was achieved. Finally, the hot solution was poured into a volumetric flask and

allowed to cool to 23 °C. The finely ground binary powder was mixed with PVA solution and sonicated at 70 °C for 90 min, periodically stirring with a glass rod. The hot mixture was cast in molds thereafter.

This method yielded the base-neutralized composites of PANI (emeraldine base form; EB). To convert PANI and its composite powders to the emeraldine salt form (ES), acid-doping was used by immersing in 1 M HCl solution and equilibration on a horizontal shaker for 24 h.

2.4. Characterization

2.4.1. ^{13}C Solid State NMR spectroscopy

^{13}C solids NMR spectra were obtained using a Bruker AVANCE III HD spectrometer operating at 125.76 MHz (^{13}C frequency). Samples were packed in 4 mm drop-in rotors and analyzed using a pulse sequence with Cross Polarization with Total Suppression of Spinning Sidebands (CP-TOSS) and a spinning frequency 7.5 kHz with a 1 ms cross-polarization time. Spectra were acquired after variable scans (n = 4 k to 4.4 k) with a recycle delay of 2 s. The ^{13}C chemical shifts (δ) were externally referenced to adamantane (δ = 38.48 ppm). Stack plots were obtained using Topspin 4.0.7 Bruker NMR software.

2.4.2. Fourier Transform Infrared (FTIR) Spectroscopy

FTIR spectra of solids were recorded using a Renishaw IlluminatIR FTIR Microscope (36× Diamond ATR Objective). IR spectra were acquired with the aid of a highly sensitive mercury cadmium telluride (MCT) detector in attenuated total reflectance (ATR) mode. The spectral range spanned from 4000 to 650 cm^{-1} with a resolution of 4 cm^{-1}. All results were baseline-corrected and normalized using Wire 5.2 software.

2.4.3. Thermal Analysis

Thermogravimetric analysis (TGA) of samples was conducted using a TA Instruments Q50 TGA system. Solid samples (ca. 10 mg) were heated from 23 to 500 °C with a heating rate of 5 °C/min under a nitrogen atmosphere. Differential scanning calorimetry (DSC) curves were acquired using a DSC TA instrument model Q20, where ca. 3 mg of sample was encapsulated in a pan and heated with a scan rate of 20 °C/min from 40 to 250 °C. The integration of the DSC endotherms and TGA peaks was carried using Origin2019 software (OriginLab Corporation, Northampton, MA, USA).

2.4.4. Swelling Tests

Swelling tests were performed by immersing each sample in a separate vial containing either pure water or an aqueous acid solution (hydrochloric or sulfuric). The samples were equilibrated for 24 h by placing them on a horizontal shaker at 150 rpm. After 24 h, they were extracted and gently blotted with a tissue to remove excess solvent. The sample weight was taken before and after equilibration in the solvent. The measurements were replicated five times using different sample portions, where the degree of swelling (%) was calculated according to Equation (1):

$$S_w = \frac{m_w - m_d}{m_d} \times 100\% \quad (1)$$

m_w is weight of swollen sample, m_d is the weight of the dry sample.

2.4.5. Adsorption Studies

The adsorption properties of the samples were studied at equilibrium and at kinetic conditions, using two types of dyes, cationic (MB) and anionic (FL).

Equilibrium Dye Uptake

Equilibrium adsorption was performed in batch mode (ca. 15 samples) in their film form with a fixed weight (ca. 10.5 ± 0.5 mg). The samples were immersed in dye solutions with variable concentration, where the MB solutions ranged from 0.1 to 5 mM and FL ranged from 20 to 500 µM. Each series of samples were allowed to equilibrate on a horizontal shaker at 150 rpm for 24 h. The optical absorbance of the respective dye solution, before and after adsorption, was measured using a Varian Cary 100 Scan UV−Vis spectrophotometer. Calibration curves were obtained for MB (λ_{max} = 664 nm) and for FL (λ_{max} = 489 nm). Equilibrium uptake (mmol/g) was calculated using Equation (2), according to differences between the final and initial concentrations at equilibrium [30]:

$$Q_e = \frac{V(C_0 - C_e)}{m} \tag{2}$$

m is the mass of polymer sample, V is the volume of MB solution, C_0 and C_e are initial and final concentrations before and after the adsorption process at equilibrium, respectively.

Adsorption isotherms were fitted to three isotherm models (cf. Figure S2 in Supplementary Materials). The Sips [31] and Freundlich [32] isotherm models assume that the surface is heterogeneous, whereas the Langmuir model [33] accounts for adsorption onto homogeneous surfaces. As seen from Figure S2 and Table S3, the Sips isotherm model provides the best-fit curve and R^2 values that lie close to unity. According to the Sips isotherm model [31], the dye uptake at equilibrium conditions was calculated by Equation (3):

$$Q_e = \frac{Q_m k_s {C_e}^{n_s}}{1 + k_s {C_e}^{n_s}} \tag{3}$$

Q_m is the monolayer adsorption capacity of material (dye uptake at saturated conditions), k_s is the Sips isotherm model constant, C_e is the equilibrium concentration of MB solution, and n_s is the Sips isotherm exponent term.

Dye adsorption was used to estimate the surface area (SA, m^2/g) of the sorbent (Equation (4)):

$$SA = \frac{Q_m \cdot N_A \cdot \sigma}{Y} \tag{4}$$

Q_m is the Sips fitting parameter from Equation (1), expressed in mol/g adsorbent, N_A is Avogadro's number (6.02×10^{23} mol^{-1}), σ is the cross-sectional molecular surface area (m^2/molecule) where σ(MB) = 8.72×10^{-19} and σ(FL) = 7.13×10^{-19}, and Y is the coverage factor (non-dimensional quantity) where Y = 2.0 for MB and FL [34,35].

Kinetics of Dye Uptake

Kinetic adsorption studies were conducted for the samples in their powder form, using a one-pot method under dynamic conditions [36]. The initial dye concentration was known (10 µM in case of MB and 15 µM for FL); its absorbance was measured within the repetitive time spans. As the initial rate of adsorption was always higher, the time spans were shorter at first (2 min) and longer at the end of the kinetic profile (40 min). The experimental data were fitted to the pseudo-first (PFO) or pseudo-second (PSO) order kinetic models (cf. Equations (5) and (6)):

$$Q_t = q_m\left(1 - e^{-k_{pfo}C_t}\right) \tag{5}$$

$$Q_t = \frac{{q_m}^2 k_{pso} C_t}{1 + q_m k_{pso} C_t} \tag{6}$$

Q_t is the amount of sorbate adsorbed by a sample (µmol/g) at a certain time (t), q_m is the maximum amount of dye (µmol/g), adsorbed at pseudo-equilibrium conditions, k_{pfo} and k_{pso} are the rate constants according to the PFO and PSO models. Experimental values of Q_t can be obtained by Equation (7),

which resembles the equilibrium form of Equation (2) except that C_t refers to the dye concentration at time (t).

$$Q_t = \frac{V(C_0 - C_t)}{m} \tag{7}$$

2.4.6. Water Vapour Adsorption

The uptake of water vapour by the sample films was done according to the method described in the literature [37]. Various atmospheric humidity levels were obtained by preparing a series of saturated salt solutions in closed glass jars. Oven-dried samples were placed inside the jars in ascending order of humidity values that underwent equilibration for 24 h. For example, salt solutions were prepared that correspond to variable relative humidity (%), as follows: LiCl (11), $MgCl_2$ (33), K_2CO_3 (43), $Mg(NO_3)_2$ (53), NaCl (71), KCl (84), and K_2SO_4 (97) [38]. The samples were gradually moved from low to higher humidity every 24 h to obtain the water vapour adsorption properties. After reaching the highest humidity level, the samples were subjected to lower humidity levels to assess their desorption properties. The sample weight was recorded at each humidity level in triplicate. The moisture content was calculated according to Equation (8):

$$\omega = \frac{m_{wet} - m_{dry}}{m_{wet}} \times 1000‰ \tag{8}$$

m_{wet} and m_{dry} are the masses of sample in the wet (at respective RH) and dry states, respectively.

2.4.7. Electrical Conductivity of Composite Materials

To investigate the behaviour of samples under an applied potential, the current–voltage behaviour of samples was recorded using a controlled voltage source device (Keithley 2420 source meter). Three specimens for each composite sample were cut out as rectangle shapes with 0.5 cm^2 area (0.5 cm × 1.0 cm) and each sample was fixed between two fastener clips. The electric current was measured at ascending tensions from 0 to 20 V with an increment of 1 V at a fixed relative humidity (64%). The raw numerical data were converted to the I–V curves using Origin2019 software and further analyzed.

2.4.8. Mechanical Properties

A dynamic mechanical analyzer (DMA 8000, PerkinElmer, Inc., Waltham, MA, USA) was used to determine the dynamic mechanical properties of the samples. Three specimens of each composite sample had a rectangular shape of ca. 8 × 20 mm^2. The tests were done using a single cantilever mode at 5 Hz frequency, and heated from 20 °C to 50 °C with a heating rate of 2 °C/min. The free length of all tests was 10.22 mm. Each sample was measured in dry and hydrated conditions. To obtain the measurements for the hydrated samples at equilibrium, samples were immersed under DI water in individual 50 mL beakers for 24 h. The sample weight and dimensions were recorded before and after water immersion.

3. Results and Discussion

3.1. ^{13}C Solid State NMR Spectroscopy

^{13}C solids NMR spectroscopy provides useful information related to the structure and composition of macromolecules and their noncovalent complexes in the solid state [39]. Herein, ^{13}C solids NMR spectroscopy was used to characterize the carbon structure of the binary and ternary composite materials. The ^{13}C spectral assignments reported herein are based on previous spectra reported for the single-component systems (chitosan, PVA, and PANI) [40–42]. Chitosan has a degree of acetylation (ca. 20%) that is supported by the presence of carbonyl and methyl groups. Pristine chitosan was reported to have the following signatures: C1 at 105.3 ppm, C4 at 83.6 ppm, C3,5 at 75.6 ppm, C6 at

60.8 ppm and C2 at 57.7 ppm [40]. C7 and C8 relate to the carbonyl and methyl groups due to the presence of acetyl groups in chitosan (see Figure S1 in the Supplementary Materials). PVA has two groups of signals that correspond to methylene (44–46 ppm) and methine (64–70 ppm) signatures [41]. It is noteworthy that methine groups of PVA overlap with C2, C3 and C6 carbons of chitosan that reside between 57 and 70 ppm. Polyaniline has aromatic signatures that occur between 120 and 160 ppm [42] that do not overlap with the spectra of chitosan or PVA. Figure 2 shows the ^{13}C NMR spectra of PANI–CHT composites with and without PVA.

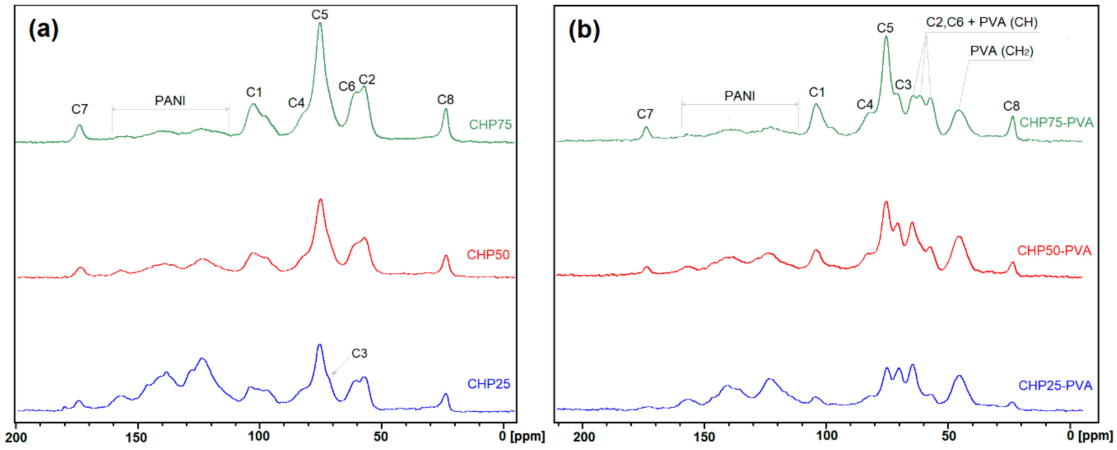

Figure 2. Solid state CP-TOSS ^{13}C NMR spectra of polymer composite materials at 295 K: (**a**) binary PANI–CHT composites; (**b**) ternary PANI–CHT–PVA composites. Spectral acquisition at the MAS frequency of 7.5 kHz with a 2 s recycle delay with 1 ms of cross-polarization.

In Figure 3, the NMR line intensities of chitosan increased from CHP25 to CHP75, while PANI line intensities showed a concomitant decrease. The C2 and C6 signatures for chitosan had constant intensity that show spectral overlap with the methine carbons of PVA, where it is difficult to assess if there are any chemical versus physical changes. Thus, the spectra do not show any unique signatures that differ from the pristine polymer. However, C3 line intensities for chitosan appear to remain constant, where it is noted that quantitative analysis is limited by the use of the CP-TOSS pulse sequence, in contrast to single-pulse experiments.

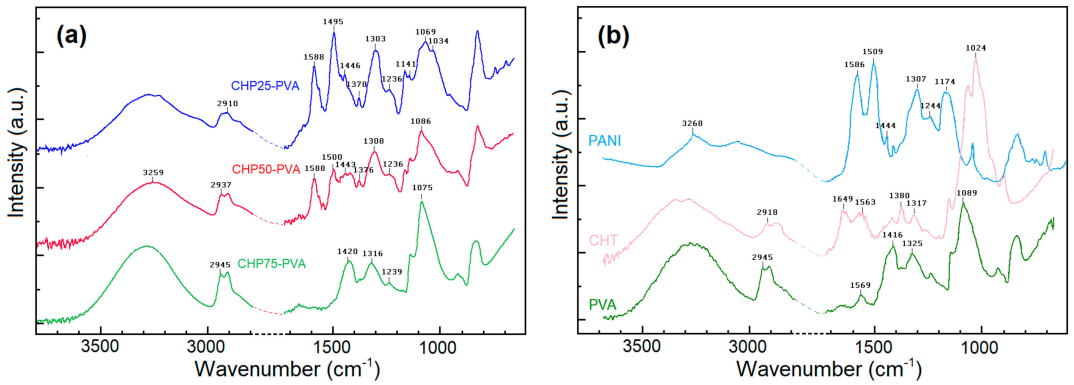

Figure 3. Normalized FTIR spectra: (**a**) ternary polymer composites with variable chitosan content; and (**b**) pristine components. The spectral region (1700–2800 cm^{-1}) was omitted for clarity.

3.2. FTIR Spectroscopy

FTIR spectroscopy provides useful information regarding a comparison of the composites versus their pristine components. IR spectral data enable determination of the presence or absence of unique functional groups, before and after composite formation. Figure 3 shows IR spectra of ternary

PANI–CHT–PVA composites. In Supplementary Materials Table S2, the IR band assignments for the precursor polymer materials are noted among the collective IR spectral signatures.

It is noteworthy that the IR spectrum of the composite with the highest chitosan content did not show notable polyaniline signals, in agreement with the reduced PANI content in the composite (i.e., benzenoid stretching at 1495–1500 cm^{-1} and quinoid stretching at 1588 cm^{-1}). By contrast, chitosan signatures show incremental intensity due to the greater chitosan content (C–H symmetric stretching at 2910 cm^{-1} and overlapping CHT–PVA signals at 1034–1086 cm^{-1}). In addition, a weak $NHCOCH_3$ signal (carbonyl from acetylated amino group) is observed. While IR results do not clearly reveal chemical interactions between the composite components, H-bonding between PANI and CHT is the most favourable interaction. PVA shows only two bands (alkyl CH and CO from alcohol) that are of similar intensity. The foregoing suggests that PVA is not involved in covalent bonding with chitosan or PANI.

3.3. Thermal Analysis

3.3.1. Thermogravimetric Analysis (TGA)

TGA is a useful tool to study the thermal stability of polymers and to estimate the composition of materials, degradation temperatures of components, and to the prevalence of cohesive interactions among components in mixed systems.

Chitosan and PVA collectively exhibit a single DTG event between 250–300 °C, [43,44] as observed in the TGA plot (Figure 4a, Figure S3). A prominent thermal event occurs between 325–400 °C due to the enhanced thermal stability of CHT–PANI–PVA composite. A higher temperature thermal event (425–500 °C) is noted with relatively low intensity that denotes the presence of PANI [29].

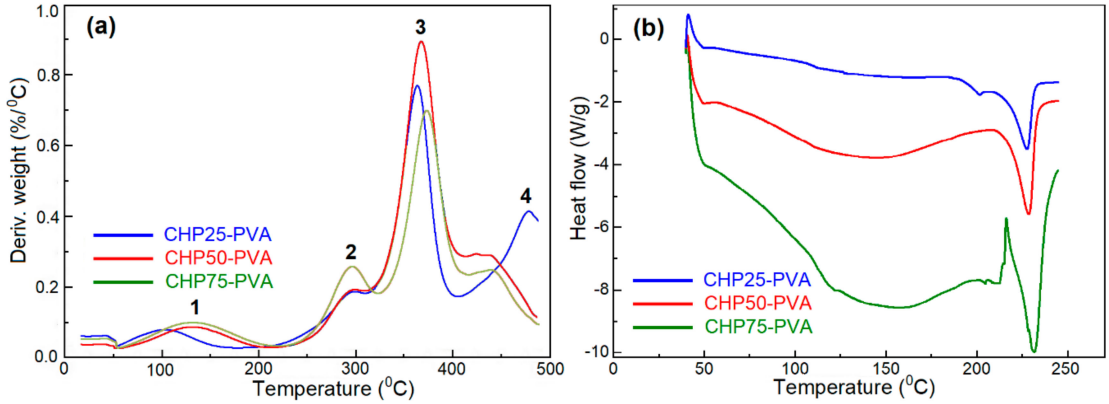

Figure 4. Thermal properties of polymer-based (PANI–CHT–PVA) composite films: (**a**) Differential thermogravimetry (DTA) profiles; and (**b**) DSC profiles (↓ endo down).

Thermal events occur in several regions as denoted by bold numbers: Region **1** (loss of water), Region **2** (decomposition of CHT and PVA), Region **3** (decomposition of polymer composite materials), and Region **4** (decomposition of PANI). The occurrence of evaporative loss of water may indicate occluded or micropore water according to a range of temperatures up to ca. 200 °C. Insight into the thermodynamic state of water can be determined from the differential scanning calorimetry (DSC) results, in addition to estimates of the enthalpy of desorption.

3.3.2. Differential Scanning Calorimetry (DSC)

Figure 4b illustrates the DSC profiles of the polymer composite materials. The profiles are characterized by two prominent endotherms; a sharp transition at ca. 230 °C and a broader thermal event from 50 to 200 °C. The sharp transition corresponds to sample melting, whereas the broad transition relates to bound water as denoted by Region **1** (cf. Figure 4a). The broad transition for the

bound water relates to the different thermodynamic states of water, as evidenced by the broad DSC transition. Figure 4b shows that the peak area is greater, especially for materials with higher chitosan content. This suggests that the enthalpy of dehydration increases as the mass fraction of chitosan increases. The trend can be accounted for, as follows: (1) stronger interactions between water molecules and the polymer components; or (2) greater levels of water incorporation within the material. These effects are indirectly supported because chitosan is hygroscopic and hydrophilic, whereas CHP75–PVA samples are observed to retain more water than CHP25–PVA (vide infra).

3.4. Solvent Swelling Tests

Solvent swelling of the single-component materials and composites occur due to sorption processes (adsorption + absorption) between the solvent and the polymer sorbent. Solvent (water) molecules penetrate into the composite microstructure and onto surface sites, where the results of solvent swelling in water or aqueous acid (HCl, H_2SO_4) solutions are listed in Table 1. Undoped samples refer to emeraldine base (EB), while doped samples correspond to the emeraldine salt (ES) form of PANI. ES samples were obtained by equilibrating the corresponding base-neutralized form of the composites in 1 M HCl solution for 24 h.

Table 1. Swelling tests of PVA/CHP 25–75 films: (**a**) with 70 wt.% content of PVA; (**b**) with 50 wt.% content of PVA.

	Swelling Properties of Samples, (w/w)%				
	Composite	**Water (*l*)**		**1 M HCl (*aq*)**	**1 M H_2SO_4 (*aq*)**
		Undoped	**Doped**	**Doped**	**Doped**
(a)	CHP25–PVA70	83 ± 2	77 ± 4	92 ± 5	93 ± 4
	CHP50–PVA70	119 ± 6	122 ± 12	98 ± 6	98 ± 5
	CHP75–PVA70	109 ± 3	228 ± 12	119 ± 11	114 ± 5
(b)	CHP25–PVA50	68 ± 2	131 ± 7	77 ± 2	82 ± 1
	CHP50–PVA50	129 ± 9	195 ± 10	119 ± 5	119 ± 5
	CHP75–PVA50	97 ± 4	210 ± 2	116 ± 2	117 ± 2

A comparison between two acid systems, HCl and H_2SO_4, was carried out to ascertain any notable differences that may account for dissolution effects, since chitosan is soluble in HCl (*aq*) but it is generally insoluble in H_2SO_4 (*aq*). The comparable swelling observed for both acid systems indicate that chitosan does not dissolve in HCl (*aq*).

The level of swelling (%) should increase for samples that possess more accessible hydrophilic groups such as –OH, –COOH, $–NH_2$, $–NHCOCH_3$, etc. Accordingly, the components of the composites listed in Table 1 possess hydrophilic character, where chitosan and PVA are among the most hydrophilic components in the composite formulation. A literature report reveals that PVA has a greater swelling contribution than chitosan [45]. For this reason, it is convenient to compare the following samples: (1) according to CHT content (series of three samples in Table 1a/b) and (2) by PVA content (cf. sections (a) and (b) in Table 1). The overall trend shows that materials with a greater CHT content show greater solvent swelling. However, there are some exclusions, as follows: CHP50 and CHP75 have 70% PVA content for swelling in water, and 50% PVA content for swelling in 1 M acid solution. The respective swelling results in acid and water are nearly equal within the limits of error. Moreover, the swelling of CHP50–PVA50 undoped samples in water is notably higher than corresponding CHP75–PVA50 samples (129% vs 97%). The variability in swelling can be accounted for by the excess content of CHT that prevents the formation of a branched and cross-linked structure that has reduced swelling. To summarize the swelling results, there are eight sets of samples (each of three specimens) that show the following trends: 83%–119%–109% (↑ and = , means to be nearly equal within an error); 77%–122%–228% (all ↑); 92%–98%–119% (↑); 93%–98%–114% (↑), 68%–129%–97% (↑ and ↓, falls out of the general trend), 131%–195%–210% (↑); 77%–119%–116% (↑ and =); 82%–119%–117% (↑ and =).

Half of the samples (4) show a clear trend: higher CHT content yields greater swelling, three samples firstly increase and then remain constant, and only one sample does not obey this rule (and even then, not for the whole set of three samples). In 75% of the cases (12 out of 16), the swelling of samples exhibit general trends, where greater CHT and PVA content yield greater swelling, along with greater cationic dye adsorption (vide infra). A comparison of doped versus undoped samples reveal greater swelling in water and moderate swelling in 1 M acid solutions. Comparable swelling was observed in aqueous HCl and H_2SO_4, where doped samples had greater swelling in pure water. This is understood due to protonation effects for the swelling process when comparing the results for water vs. aqueous acid solutions. Chitosan is insoluble in H_2SO_4 (*aq*), but it may have partial solubility in HCl (*aq*). The similar level of solvent swelling in both acid media rules out the dissolution of chitosan.

3.5. Equilibrium and Kinetic Dye Uptake

Equilibrium swelling was carried out for the ternary composite films, while the kinetic uptake for the binary composites was studied for powdered samples. This approach was undertaken due to the following: (1) effective conversion of films into uniform powders with a conventional mortar and pestle has limitations; (2) batch adsorption requires an additional phase separation step with powders, involving an additional operation (e.g., filtration or centrifugation); (3) the one-pot kinetic method is suitable for the study of powdered materials. The adsorption results for samples in film and powder forms should follow parallel trends in adsorption.

3.5.1. Methylene Blue (MB) Adsorption

Equilibrium Dye Uptake

MB was used as a dye probe to study the adsorption properties of materials under equilibrium and kinetic conditions. The ternary sorbents in their film form adsorbed MB according to the isotherm profiles shown in Figure 5a, where MB solutions with greater decolorization correspond to samples with greater dye uptake. Figure 5a shows that composite samples with variable chitosan content had greater adsorption capacity, as follows: CHP75–PVA > CHP50–PVA > CHP25–PVA.

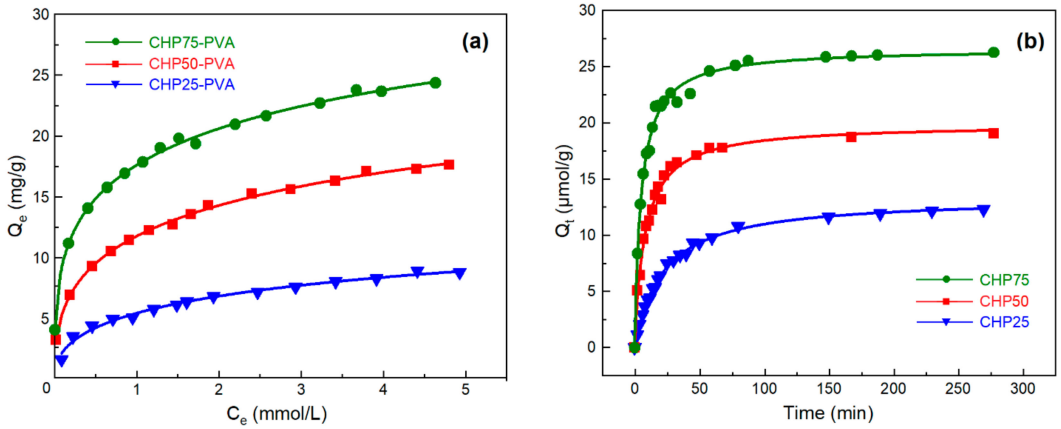

Figure 5. Equilibrium dye uptake of methylene blue by PANI-based composite materials at 298 K and pH 7: (**a**) equilibrium isotherm according to the Sips model in their film form; (**b**) kinetic profiles fitted to the pseudo-second order (PSO) model for the powdered samples.

The monolayer uptake capacity (Q_m) can be calculated according to the type of adsorption isotherm (Langmuir, Freundlich and Sips) models in Supplementary Materials Table S3. The best-fit results are shown by the Sips isotherm model with the correlation coefficients (R^2) that lie closer to unity (Table 2). The SA of the materials was estimated from the best-fit adsorption parameters by the Sips model (Table 2). Table 2 lists a comparison of the adsorption capacities of single components

(CHT and PANI) and binary composite CHT/PANI materials [29,46], where the Q_m values for ternary films are slightly higher than the Q_m values for the pristine components.

Table 2. Sips isotherm parameters: monolayer adsorption capacity (Q_m) and accessible surface area (SA) for ternary/binary composites and single component materials. [1]

Sorbent	Q_m(mg/g)	k_s (L/mmol)	n_s	R^2	SA (m^2/g) [1]	Reference
CHP25–PVA	19.1	0.382	0.492	0.986	15.7	This work
CHP50–PVA	37.8	0.444	0.430	0.998	31.0	This work
CHP75–PVA	51.5	0.512	0.362	0.998	42.3	This work
CHT	3.84	—	1.52	0.977	—	Ref. [47]
PANI	34.9	1.68	—	—	—	Ref. [29]
CHT/PANI	20.0	1.37	—	—	—	Ref. [29]

[1] Based on the equilibrium uptake of MB (methylene blue) as the dye probe

A clear trend for the MB adsorption data is observed, whereby the values for Q_m and SA of the composites increase as the chitosan content increases. This trend can be explained by the role of cross-linking and the favourable MB dye adsorption properties of chitosan. The increase in the SA of the adsorbent parallels the trend in results for the estimated density values. As seen from Supplementary Materials Table S4, the density of the composite gradually decreases with increasing chitosan content. The decreasing trend in composite density may add further evidence that the greater porosity noted for CHP75–PVA provides an account of its greater SA and dye uptake properties, as compared with the other ternary composites.

By contrast, the theoretical densities listed in Table S4 have greater values, as compared with the experimental results. The density results indicate that the ternary composite film is not just a physical mixture but also forms a uniquely structured composite with a well-defined pore structure.

Dye Uptake Kinetics

The kinetic uptake of MB by the PANI-based composites is shown in Figure 5b. The overall trend reveals that rapid adsorption occurs during the first 25 min of the isotherm profile, where reduced uptake occurs thereafter. The greater adsorption during the first stage is accounted for by the presence of more accessible surface sites, whereas subsequent uptake is reduced due to saturation of the remaining surface and/or uptake at micropore domains where slower diffusion occurs.

The kinetic profiles are well-described by the pseudo-second order (PSO) model (cf. Figure S4 in Supplementary Materials), in agreement with correlation coefficients (R^2) near unity. As shown in Table 3, the general trends for the maximum kinetic uptake (q_m) are paralleled by the trends for the equilibrium uptake, where greater adsorption occurs as the mass fraction of chitosan in the composite increases.

Table 3. Kinetic adsorption parameters of MB with different sorbents in their powder form.

Sorbent	q_m (μmol/g)	k_{pso} (g·μmol^{-1}·min^{-1})	R^2	Reference
CHP25	13.4	0.00343	0.998	This work
CHP50	19.9	0.00635	0.990	This work
CHP75	26.6	0.00748	0.993	This work
CHT	2.69	0.0259	0.969	This work
PANI	22.7	—	—	Ref. [29]
CHT/PANI	15.4	—	—	Ref. [29]

The adsorption capacities of pristine components at pseudo-equilibrium conditions from the kinetic isotherms follow similar trends as the isotherms at equilibrium conditions. Pristine chitosan displays relatively poor adsorption with respect to its binary composites. In a study reported by Mohamed et al. [29], a binary composite of CHT and PANI showed similar adsorptive capacity to those

prepared herein. The values of k_{pso} for the composites (CHP25–CHP50–CHP75) gradually increase in a parallel fashion, similar to the adsorption capacities listed in Table 3.

The trends for the equilibrium and kinetic uptake of MB revealed several effects: greater cross-linking and chitosan content increased the textural properties; diffusion effects in a pore system were reduced as the contact time of the adsorbent-adsorbate system increased.

3.5.2. Fluorescein (FL) Adsorption

Equilibrium Dye Uptake

PANI-based composites display favourable adsorption properties toward MB, a cationic dye that is suitable for probing heteroatom sites with abundant electron density. Complementary adsorption isotherms were obtained using an anionic dye (fluorescein; FL) to assess the presence of active sites with Lewis acid character in the composite materials. Ternary PANI-based films were prepared in their base-neutralized form that were initially isolated as the emeraldine base (EB) form. Thus, it was of particular interest to acid-dope the composites to assess whether protonation would contribute enhanced dye adsorption of anions. The contribution of electrostatic effects between acid-doped PANI was hypothesized to result in greater dye uptake of FL relative to the undoped composite. The effect of acid doping was confirmed by visual observation, where fluorescein at variable concentration (up to 150 μM; samples 501–509) underwent complete decolorization (cf. Figure S5 in Supplementary Materials).

Furthermore, the undoped (base-neutralized) films were also tested. The comparative chart depicts the FL uptake by the doped films (indexed as "doped") versus undoped samples at equilibrium conditions—shown in Figure 6a. Accordingly, the corresponding surface area of the sorbent was estimated from the results in Table 4.

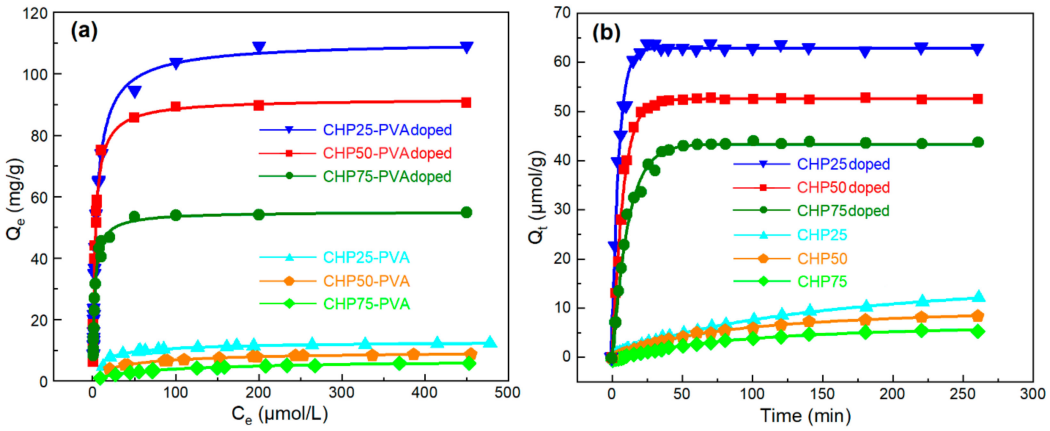

Figure 6. Equilibrium dye uptake of fluorescein by PANI-based composite materials at 298 K and pH 7: (**a**) equilibrium isotherm according to the Sips model in their film form; (**b**) kinetic profiles fitted to the pseudo-first (PFO) for the doped specimens and to pseudo-second order (PSO) model for undoped samples in their powder form.

As shown in Tables 2 and 4, there was a reversal in the trend for FL adsorption, as compared to that for MB adsorption. A lower chitosan content led to a greater uptake of FL, in accordance with the higher PANI content for samples with low-chitosan content. This indicates that the greater number of positively charged amine sites attract negatively charged dye molecules. However, both PANI and chitosan are susceptible to acid doping, where similar trends for uptake of MB may not apply, as noted for fluorescein. On the other hand, undoped PANI-based species reveal higher uptake of a MB cation rather than a FL anion, where a maximum 7-fold difference is noted in Tables 2 and 4, where CHP25 displayed the highest FL uptake in either its doped and undoped forms. In contrast, the undoped species display ca. 10-fold lower Q_m values versus the doped composites. By contrast, pristine chitosan

has negligible adsorption, in agreement with other reports [29,35]. Regarding the adsorptive properties towards FL with pristine PANI, no relevant literature data were found, revealing a knowledge gap for such dye systems in this field of polymer adsorbents. However, other reports [47,48] reveal that undoped PANI favours adsorption of cationic dyes over anionic dyes, in parallel agreement with the trends reported herein.

Table 4. Sips isotherm parameters, adsorption capacity (Q_m) and accessible surface area (SA) for pristine chitosan and ternary composite films in their acid-doped/ base-neutralized forms. [1]

Sorbent	Q_m (mg/g)	k_s(L/μmol)	n_s	R^2	SA (m^2/g) [1]	Reference
CHP25-PVAdoped	110.9	0.295	0.837	0.997	63.3 *	This work
CHP50–PVAdoped	92.0	0.390	0.881	0.997	52.5 *	This work
CHP75–PVAdoped	55.1	0.525	0.891	0.995	31.4 *	This work
CHP25–PVA	13.6	0.0152	0.627	0.993	7.73	This work
CHP50–PVA	10.2	0.0109	0.730	0.997	5.82	This work
CHP75–PVA	7.68	0.00560	0.748	0.982	4.38	This work
CHT	1.96	—	—	—	—	[35]

[1] Based on the equilibrium uptake of FL (fluorescein) as the dye probe. * Denotes the contribution of electrostatic interactions that may potentially skew the results of SA determination; however, the general trend will remain unchanged for such acid doped samples.

Kinetic Dye Uptake

Figure 6b outlines the uptake of FL by the PANI–CHT binary powders at kinetic conditions. While these composites do not contain PVA, the general trend shows a similar correspondence with the isotherm results obtained at equilibrium conditions. Table 5 shows kinetic parameters of the doped powders versus undoped binary composites. In the case of doped composites, the PFO model was tested, whereas the PSO kinetic model was found to be more suitable for describing the kinetic profiles of the undoped composite materials.

Table 5. Kinetic adsorption parameters of FL with the doped and undoped sorbents in their powdered form.

Sorbent	q_m(μmol/g)	k_{pfo}(min^{-1})	k_{pso}(g·μmol^{-1}·min^{-1})	R^2
CHP25doped	62.9	0.216	—	0.993
CHP50doped	52.7	0.139	—	0.995
CHP75doped	43.5	0.0925	—	0.993
CHP25	18.8	—	0.00139	0.999
CHP50	11.3	—	0.00113	0.998
CHP75	8.46	—	0.000322	0.996

At a glance, the kinetic adsorption models indicate that the acid-doped samples favour physisorption (PFO), while the undoped samples obey the chemisorption mechanism (PSO) [49]. However, the intermolecular interactions are stronger in the case of doped samples (due to electrostatic forces) and should facilitate chemisorption. The origin of this discrepancy is understood since the adsorption mechanism cannot be determined solely by the fitting results. The adsorption process is far more complex and altered by diffusion effects of the solute into the adsorbent.

3.6. Water Vapour Adsorption

PANI-based films have hydrophilic character that should be sensitive towards ambient humidity. The sample weight gain of film varies as the relative humidity (RH) increased, according to the presence of different inorganic salt solutions. The equilibrium vapour pressure (RH) over the salt solution depends on the nature of salt, resulting in variable RH values for different salt solutions, as described

elsewhere [37]. The saturated salts solutions were used to cover a range of RH values. The samples were initially dried prior to exposure to an RH vapour of 11% over a LiCl solution. After 24 h of equilibration, the sample was removed and equilibrated at the next incremental RH, along with the change in sample weight, until the maximal value was achieved. The samples were likewise exposed to lower RH values in descending order to establish the desorption profile over a range of humidity values from 11% to 97% (Figure 7).

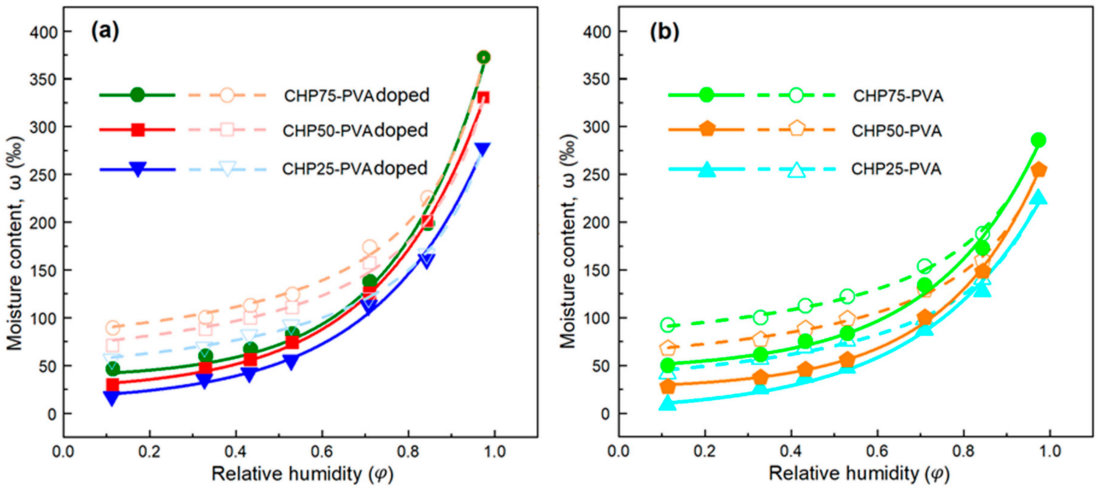

Figure 7. Isothermal moisture adsorption (solid line) and desorption (dotted line) properties of films versus relative humidity at room temperature: (**a**) for the acid-doped films; (**b**) for the base-neutralized films.

Equation (9) represents the corresponding exponential correlation of the moisture adsorption by films.

$$\omega = e^{a+b\varphi} \tag{9}$$

ω is the moisture content in %; a and b are parameters of the exponential function; and φ is a relative humidity expressed in non-dimensional relative units (not as % values).

The moisture desorption law somewhat differs from the adsorption relation since it is represented by the reciprocal function denoted by Equation (10).

$$\omega = \frac{1}{c + d\varphi} \tag{10}$$

The terms, ω and φ, have similar meaning as in Equation (9); where c and d are non-dimensional parameters of the reciprocal equation.

Supplementary Materials Table S6 represents parameters for the fitting curves and the moisture content ω_{max} at the highest RH (97%), depending on the formulation of the composite films. The values of the free parameters are similar, where the approximate magnitude ranges, as follows: $1 < a < 2$ and $4 < b < 5$ for the adsorption process. By comparison, $0.02 < c < 0.03$ and d is always negative (≈ -0.02) for the desorption process. This implies that the moisture adsorption–desorption mechanism for all of the films are similar. On the other hand, the quantity of adsorbed water vapour increases as the chitosan content increases that parallels the trend noted for the MB adsorption. This can be accounted for by increasing the number of active sites (surface area) of the sorbent, where an increased chitosan content yields a more branched and cross-linked structure. Doped films adsorb ca. 30 to 100% more moisture, relative to the undoped analogues. This result is in good correspondence with the trends in FL adsorption herein. As the water molecules possess partial negative electrostatic charge on oxygen, adsorption occurs at the positively charged nitrogen of PANI for its emeraldine salt form.

3.7. Electrical Conductivity

Electrical conductivity of samples was estimated from the I–V curve results that illustrate the relationship between the current and the applied voltage through the sample. PANI-based samples in their film form were produced with two types of PANI: EB and ES. The EB form resulted in non-conductive films, whereas ES showed a weak conductivity at low current values. The main conductive component in these films is the PANI ES fraction that has been widely reported [14]. By contrast, PANI in its EB form is a semiconductor, while the ES form of PANI is conductive [50,51]. In this work, the EB form of PANI was non-conductive due to the high content of PVA, a non-conductive polymer used in ternary film preparation. The presence of PVA led to greater electrical resistance of the film. A conductive polymer should reach a certain value of the "percolation threshold" [52] in order to impart conductivity. For a significant quantity of non-conductive polymer, this threshold is also high. Thus, only small electrical currents can pass through ES samples. However, altering the PVA content in the composites led to a marked change in conductivity, as shown in Figure 8.

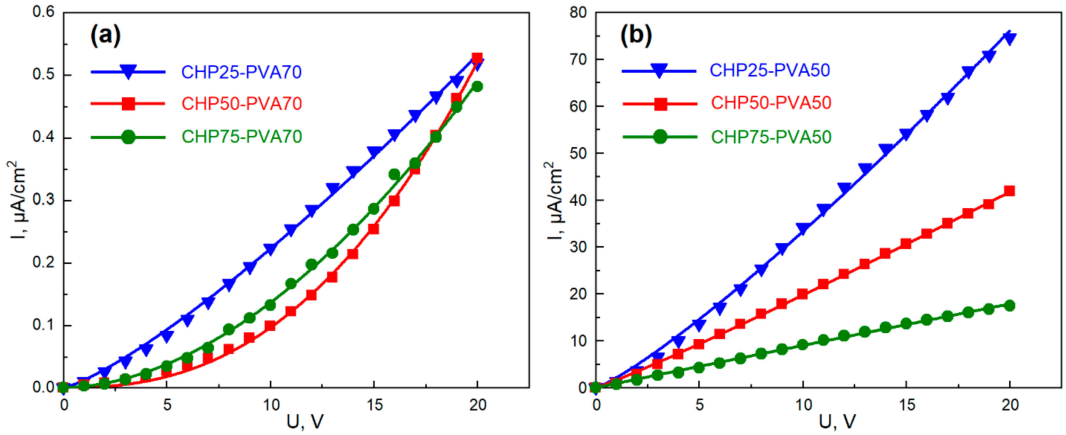

Figure 8. Current–voltage characteristics of the acid-doped PANI-based films: (**a**) with 70% w/w content of PVA; (**b**) with 50% w/w content of PVA.

When the PVA content was reduced by 20%, the conductivity showed a 100-fold improvement. On the other hand, when the PVA content decreased, the dependence appeared to be more linear. For ideal cases, the current is described by Equation (11):

$$I = KU \tag{11}$$

I is the current in Amps and U is the tension measured in Volts. K is a constant referred to as the conductance, where the magnitude of this physical quantity is the inverse of resistance, where $K = 1/R$ and $[R] = \Omega$. When a material exhibits a non-linear behaviour for I, Equation (11) transforms to the power function (cf. Equation (12)):

$$I = KU^{\beta} \tag{12}$$

β is a non-linear factor, where Supplementary Materials Table S7 shows non-linear factors together with the correlation coefficients R^2 for each curve. In case (a), the non-linear factor is significant and varies from 1.3 to 2.4; whereas for case (b), the I–V curve is subject to a linear behaviour with β values between 1.0 and 1.2. This suggests that with a lower PVA content, the I–V dependence becomes almost linear and is typical for conductors such as metals. When the PVA content increases, the line significantly deviates from the linear form, where such behaviour is typical for semiconductors such as diodes and thyristors. Comparing the current flow through the samples with various CHT content, it is noted that higher content of chitosan (with lower content of PANI) resulted in decreased conductivity (κ), as listed in Table 6. This concurs with the non-conductive nature of chitosan and the conducting properties of PANI.

Table 6. Conductivity of the composite films, calculated as a slope of the linear function.

Sample	κ (μS/cm)	R^2
CHP25–PVA50	3.92 ± 0.05	0.996
CHP50–PVA50	2.12 ± 0.01	0.999
CHP75–PVA50	0.90 ± 0.01	0.998

3.8. Mechanical Properties

Mechanical properties of the composite materials were measured using Dynamic Mechanical Analysis (DMA). DMA is a powerful technique which allows for determination of the viscoelastic behaviour of a sample under variable temperature conditions. The general ability to resist the deformation is measured by a complex modulus that consists of the Young's storage and loss moduli (E′ and E″), respectively. The storage modulus (E′) is a measure of elastic behaviour of a material, and provides a measure of the stored energy that is responsible for the elastic portion. The loss modulus (E″) is responsible for the viscous portion in the material and measures the energy dissipated during the sinusoidal deformation. Both loss and storage moduli tend to decrease with increased temperature, where less force is required to deform the sample. However, it is the storage modulus that has direct relation to the material stiffness (higher E′—higher stiffness). In contrast, the loss modulus is not directly proportional to the material stiffness. When the material reaches its glass transition temperature (T_g), the molecular friction increases and dissipates the applied force. At the T_g value of the material, the loss modulus increases while the storage modulus rapidly declines (as the dissipated energy surpasses the stored energy). This can be observed for the sample CHP75–PVA (cf. Figure 9a and Figure S6, Ia).

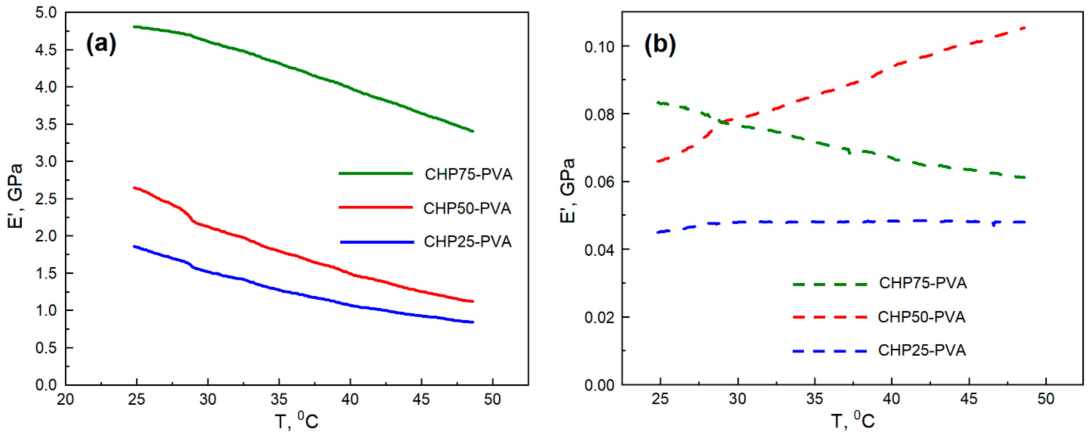

Figure 9. Relationship between the storage modulus and temperature of the base-neutralized films in their (**a**) dry, and (**b**) wet states.

Figure 9 illustrates the DMA properties of the CHP–PVA films, based on their chitosan content, and in their dry or wet states. The general trend showed the elastic modulus E′ increased (with an increase in the material stiffness) as the chitosan content was augmented. This may imply that when the chitosan sample content increased, a more cross-linked network structure is created that results in the so-called "pillaring effect" [53]. As the sample is exposed to moisture, the trends in the change of the storage modulus become altered. For example, the CHP75–PVA composite samples decreased their storage modulus, while the CHP50–PVA composites showed an increase in storage modulus, while CHP25–PVA composites have a relatively constant storage modulus. Such behaviour can be explained when water is imbibed within the sample structure it diminishes its stiffness, resulting in the storage of more energy and an increase in the elastic modulus. The CHP50–PVA composite sample

displayed similar behaviour in its wet state, where both the loss and storage moduli increased with elevated temperature.

Another interesting observation relates to the maxima in the loss modulus graphs, as shown in Figure S6 (I). The sharp energy dissipation emphasizes that the sample reached its respective T_g value. For instance, the T_g value for CHP50–PVA (dry state, one sample) and CHP75–PVA (wet state, two samples) were 41 °C and (27 °C and 31 °C), respectively. The glass transitions can be seen for both E′ and tanδ (tan delta) graphs, as shown in Figure S6 (II). The tan delta, or the damping factor, is measured as the ratio of E″/E′ and its trends are depicted in Figure S6, Section II. In general, the loss tangent factor is inversely proportional to the storage modulus. For this reason, CHP25–PVA had the lowest E′ (and stiffness) and the highest tan delta (cf. Figure 9a, and Figure S6, IIa in the Supplementary Materials).

Regardless of the behaviour of the wet composite samples at elevated temperature, the room temperature storage modulus had a similar performance to the dry samples, as shown in Figure 9b. For example, the storage modulus trend was CHP75–PVA > CHP50–PVA > CHP25–PVA. The loss tangent factor shows a reverse trend, as follows: CHP75–PVA < CHP50–PVA < CHP25–PVA. It is also noteworthy that the loss and storage moduli for wet composite samples were almost two orders of magnitude less than that for dry composites. This comparison suggests that the rigidity dropped by almost 100-fold when the samples became hydrated.

4. Conclusions

Several unique ternary PANI–CHT–PVA composites were prepared via a simple and low-cost synthetic method that employed noncovalent cross-linking and physical blending. NMR and IR spectroscopy confirmed the presence of the components, where it was inferred that cross-linking occurs between CHT and PANI via hydrogen bonding, while PVA forms weak nonspecific interactions. TGA profiles of the composites displayed a unique thermal event that was absent for the pristine components, in agreement with the formation of polymer composites. DSC showed a broad endotherm region related to the water sorption at micropore and surface sites, where the effect was more pronounced at higher CHT content. Cationic and anionic dye adsorption showed a reversal of trends for dye uptake by the composites: MB uptake increased as the chitosan content of the composites increased, whereas a decreased adsorption capacity was shown for FL uptake. Acid-doped films showed greater FL uptake, in comparison with their undoped analogues. Water swelling for CHP75–PVA samples was the highest, where the trend for incremental swelling revealed by DSC profiles parallel the MB uptake results. The acid-doped samples showed a clear incremental trend in conductivity with decreased weight fraction of chitosan. Reducing the incorporation of the non-conductive PVA (by 20 wt.%) resulted in ca. *100-fold* increase in the conductivity (and in some cases significantly reduced swelling), whereas the undoped samples are generally non-conductive. Mechanical properties reveal that the highest modulus for the composites with greater chitosan content concur with the trends in solvent swelling and MB adsorption. On the other hand, the storage modulus of wet samples dramatically decreased in comparison to their dry analogues.

Supplementary Materials: The following are available online at http://www.mdpi.com/2504-477X/4/1/18/s1, Figure S1: Numbering assignment scheme of chitosan ^{13}carbon atoms, Figure S2: Fitting lines for (CHP25-PVA, CHP50-PVA and CHP75-PVA) MB equilibrium uptake according to the various isotherm models, Figure S3: Thermogravimetry profiles of pristine components – PANI, CHT and PVA, Figure S4: Fitting lines for (CHP25-PVA, CHP50-PVA, CHP75-PVA and pristine CHT) MB kinetic uptake according to the PFO and PSO models, Figure S5: Batch adsorption experiment that illustrates decolorization of FL solutions by the PANI-based adsorbent at pH 7, Figure S6: DMA mechanical properties of the base-neutralized films in their (a) dry, and (b) wet state; Table S1: List of shorthand notation used in this study, Table S2: FTIR bands of PANI-CHT-PVA composites, Table S3: Error bars for the adsorption experiments shown in Figure S2, Table S4: Mean densities of polymer composite materials based on geometric volume determination of the film, Table S5: Error bars for the adsorption experiments shown in Figure S4, Table S6: Water vapor adsorption parameters of the doped and undoped composites in their film form, Table S7: Current-voltage parameters for the I-V curves of samples in their film form.

Author Contributions: Conceptualization, L.D.W.; methodology, Y.A.A. and L.D.W.; formal analysis, Y.A.A.; investigation, Y.A.A.; resources, L.D.W and D.E.C.; data curation, Y.A.A.; writing—original draft preparation, Y.A.A.; writing—review and editing, Y.A.A., L.D.W. and D.E.C.; visualization, Y.A.A.; supervision, L.D.W. and D.E.C.; project administration and funding acquisition, L.D.W. All authors have read and agreed to the published version of the manuscript.

Funding: L.D.W. acknowledges the support by the Government of Canada through the Natural Sciences and Engineering Research Council of Canada (Discovery Grant Number: RGPIN 2016-06197).

Acknowledgments: Professor Richard Evitts at the University of Saskatchewan is acknowledged for providing access to the facility for measurement of water vapour adsorption at variable humidity.

Conflicts of Interest: The authors declare no conflict of interest.

References

1. Li, D.; Huang, J.; Kaner, R.B. Polyaniline Nanofibers: A Unique Polymer Nanostructure for Versatile Applications. *Acc. Chem. Res.* **2009**, *42*, 135–145. [CrossRef] [PubMed]
2. Eskandari, E.; Kosari, M.; Farahani, M.H.D.A.; Khiavi, N.D.; Saeedikhani, M.; Katal, R.; Zarinejad, M.; Saeeidikhani, M. A review on polyaniline-based materials applications in heavy metals removal and catalytic processes. *Sep. Purif. Technol.* **2020**, *231*, 115901. [CrossRef]
3. Genies, E.; Boyle, A.; Lapkowski, M.; Tsintavis, C. Polyaniline: A historical survey. *Synth. Met.* **1990**, *36*, 139–182. [CrossRef]
4. Paul, E.W.; Ricco, A.J.; Wrighton, M.S. Resistance of polyaniline films as a function of electrochemical potential and the fabrication of polyaniline-based microelectronic devices. *J. Phys. Chem.* **1985**, *89*, 1441–1447. [CrossRef]
5. Ramamurthy, P.; Malshe, A.; Harrell, W.; Gregory, R.; McGuire, K.; Rao, A. Polyaniline/single-walled carbon nanotube composite electronic devices. *Solid-State Electron.* **2004**, *48*, 2019–2024. [CrossRef]
6. Yang, L.; Qiu, W.; Liu, Q. Polyaniline cathode material for lithium batteries. *Solid State Ion.* **1996**, *86*, 819–824. [CrossRef]
7. Shi, H.-Y.; Ye, Y.-J.; Liu, K.; Song, Y.; Sun, X. A Long-Cycle-Life Self-Doped Polyaniline Cathode for Rechargeable Aqueous Zinc Batteries. *Angew. Chem. Int. Ed.* **2018**, *57*, 16359–16363. [CrossRef]
8. Irimia-Vladu, M.; Fergus, J.W. Suitability of emeraldine base polyaniline-PVA composite film for carbon dioxide sensing. *Synth. Met.* **2006**, *156*, 1401–1407. [CrossRef]
9. Anju, V.P.; Jithesh, P.R.; Narayanankutty, S.K. A Novel Humidity and Ammonia Sensor Based on Nanofibers/Polyaniline/Polyvinyl Alcohol. *Sens. Actuators A Phys.* **2019**, *285*, 35–44. [CrossRef]
10. Tanguy, N.R.; Arjmand, M.; Yan, N. Nanocomposite of Nitrogen-Doped Graphene/Polyaniline for Enhanced Ammonia Gas Detection. *Adv. Mater. Interfaces* **2019**, *6*, 1900552. [CrossRef]
11. Sapurina, I.; Stejskal, J. The mechanism of the oxidative polymerization of aniline and the formation of supramolecular polyaniline structures. *Polym. Int.* **2008**, *57*, 1295–1325. [CrossRef]
12. Pud, A.; Ogurtsov, N.; Korzhenko, A.; Shapoval, G. Some aspects of preparation methods and properties of polyaniline blends and composites with organic polymers. *Prog. Polym. Sci.* **2003**, *28*, 1701–1753. [CrossRef]
13. Sedaghat, S. Synthesis and Evaluation of Chitosan-Polyaniline Copolymer in Presence of Ammonium Persulfate as Initiator. *J. Appl. Chem. Res.* **2014**, *8*, 47–54.
14. Wallace, G.G.; Teasdale, P.R.; Spinks, G.M.; Kane-Maguire, L.A.P. *Conductive Electroactive Polymers*; Informa UK Limited: Colchester, UK, 2008; pp. 137–194.
15. Liu, G.; Freund, M.S. New Approach for the Controlled Cross-Linking of Polyaniline: Synthesis and Characterization. *Macromolecules* **1997**, *30*, 5660–5665. [CrossRef]
16. Li, J.; Zhu, L.; Wu, Y.; Harima, Y.; Zhang, A.; Tang, H. Hybrid composites of conductive polyaniline and nanocrystalline titanium oxide prepared via self-assembling and graft polymerization. *Polymer* **2006**, *47*, 7361–7367. [CrossRef]
17. Acevedo, D.F.; Salavagione, H.J.; Miras, M.C.; Barbero, C.A. Synthesis, Properties and Applications of Functionalized Polyanilines. *J. Braz. Chem. Soc.* **2005**, *16*, 259–269. [CrossRef]
18. Florea, L.; Lahiff, E.; Diamond, D. Modified Polyaniline Nanofibres for Ascorbic Acid Detection. *MRS Proc.* **2011**, *1312*, 131–135. [CrossRef]
19. Lahiff, E.; Woods, T.; Blau, W.; Wallace, G.G.; Diamond, D. Synthesis and Characterisation of Controllably Functionalised Polyaniline Nanofibres. *Synth. Met.* **2009**, *159*, 741–748. [CrossRef]

20. Cheng, D.; Xia, H.; Chan, H.S. Synthesis and Characterization of Surface-Functionalized Conducting Polyaniline-Chitosan Nanocomposite. *J. Nanosci. Nanotechnol.* **2005**, *5*, 466–473. [CrossRef]
21. Janaki, V.; Vijayaraghavan, K.; Oh, B.-T.; Ramasamy, A.K.; Kamala-Kannan, S. Synthesis, Characterization and Application of Cellulose/Polyaniline Nanocomposite for the Treatment of Simulated Textile Effluent. *Cellulose* **2013**, *20*, 1153–1166. [CrossRef]
22. Aoi, K.; Takasu, A.; Okada, M. New Chitin-Based Polymer Hybrids. 2. Improved Miscibility of Chitin Derivatives Having Monodisperse Poly(2-methyl-2-oxazoline) Side Chains with Poly(vinyl chloride) and Poly(vinyl alcohol)1. *Macromolecules* **1997**, *30*, 6134–6138. [CrossRef]
23. Pires, C.T.; Vilela, J.A.; Airoldi, C. The Effect of Chitin Alkaline Deacetylation at Different Condition on Particle Properties. *Procedia Chem.* **2014**, *9*, 220–225. [CrossRef]
24. Czechowska-Biskup, R.; Jarosińska, D.; Rokita, B.; Ulański, P.; Rosiak, J.M. Determination of Degree of Deacetylation of Chitosan—Comparison of Methods. In *Progress on Chemistry and Application of Chitin and Its Derivatives*; Lodz University of Technology: Lodz, Poland, 2012; Volume XVII, pp. 5–20.
25. Timur, M.; Paşa, A. Synthesis, Characterization, Swelling, and Metal Uptake Studies of Aryl Cross-Linked Chitosan Hydrogels. *ACS Omega* **2018**, *3*, 17416–17424. [CrossRef] [PubMed]
26. Li, W.; Jang, D.M.; An, S.Y.; Kim, D.; Hong, S.-K.; Kim, H. Polyaniline–chitosan nanocomposite: High performance hydrogen sensor from new principle. *Sensors Actuators B Chem.* **2011**, *160*, 1020–1025. [CrossRef]
27. Wang, X.H.; Mu, Y.H.; Li, C.Q.; Nie, M.; Hua, W.X.; Hua, M.Y.; Qiang, L.C.; Ming, N. Preparation of PANI–PVA composite film with good conductivity and strong mechanical property. *Plast. Rubber Compos.* **2015**, *44*, 345–349. [CrossRef]
28. Chauhan, N.P.S. Chapter 11—Functionalized Polyaniline and Composites. In *Fundamentals and Emerging Applications of Polyaniline*; Elsevier, Inc.: Cambridge, MA, USA, 2019; pp. 177–201.
29. Mohamed, M.H.; Dolatkhah, A.; Aboumourad, T.; Dehabadi, L.; Wilson, L.D. Investigation of templated and supported polyaniline adsorbent materials. *RSC Adv.* **2015**, *5*, 6976–6984. [CrossRef]
30. Sun, Q.; Yang, L. The adsorption of basic dyes from aqueous solution on modified peat–resin particle. *Water Res.* **2003**, *37*, 1535–1544. [CrossRef]
31. Sips, R. On the Structure of a Catalyst Surface. *J. Chem. Phys.* **1948**, *16*, 490. [CrossRef]
32. Freundlich, H.M.F. Über die Adsorption in Lösungen. *J. Phys. Chem. A* **1906**, *57*, 385–470. [CrossRef]
33. Langmuir, I. The adsorption of gases on plane surfaces of glass, mica and platinum. *J. Am. Chem. Soc.* **1918**, *40*, 1361–1403. [CrossRef]
34. Sabzevari, M.; Wilson, L.D.; Cree, D.E. Gas and Solution Uptake Properties of Graphene Oxide-Based Composite Materials: Organic vs. Inorganic Cross-Linkers. *J. Compos. Sci.* **2019**, *3*, 80. [CrossRef]
35. Vafakish, B.; Wilson, L.D. Surface-Modified Chitosan: An Adsorption Study of a "Tweezer-Like" Biopolymer with Fluorescein. *Surfaces* **2019**, *2*, 468–484. [CrossRef]
36. Mohamed, M.H.; Wilson, L.D. Kinetic Uptake Studies of Powdered Materials in Solution. *Nanomaterials* **2015**, *5*, 969–980. [CrossRef] [PubMed]
37. Chen, H.; Evitts, R.W.; Besant, R.W. Moisture adsorption characteristics of a thin bed of polycrystalline potash pellets. *Powder Technol.* **2006**, *170*, 158–166. [CrossRef]
38. Greenspan, L. Humidity fixed points of binary saturated aqueous solutions. *J. Res. Natl. Bur. Stand. Sect. A Phys. Chem.* **1977**, *81*, 89. [CrossRef]
39. Wang, T.; Hong, M. Solid-State NMR Investigations of Cellulose Structure and Interactions with Matrix Polysaccharides in Plant Primary Cell Walls. *J. Exp. Bot.* **2016**, *67*, 503–514. [CrossRef]
40. Mahaninia, M.H.; Wilson, L.D. Modular Cross-Linked Chitosan Beads with Calcium Doping for Enhanced Adsorptive Uptake of Organophosphate Anions. *Ind. Eng. Chem. Res.* **2016**, *55*, 11706–11715. [CrossRef]
41. Katsuraya, K.; Hatanaka, K.; Matsuzaki, K.; Amiya, S. Assignment of finely resolved ^{13}C NMR spectra of poly(vinyl alcohol). *Polymer* **2001**, *42*, 9855–9858. [CrossRef]
42. Zujovic, Z.D.; Bowmaker, G.A.; Tran, H.D.; Kaner, R.B. Solid-state NMR of polyaniline nanofibers. *Synth. Met.* **2009**, *159*, 710–714. [CrossRef]
43. Kim, S.J.; Park, S.J.; Kim, I.Y.; Lee, Y.H.; Kim, S.I. Thermal Characteristics of Poly(vinylalcohol) and Poly(vinylpyrrolidone) IPNs. *J. Appl. Polym. Sci.* **2002**, *86*, 1844–1847.
44. Udoetok, I.A.; Wilson, L.D.; Headley, J.V. Self-Assembled and Cross-Linked Animal and Plant-Based Polysaccharides: Chitosan–Cellulose Composites and Their Anion Uptake Properties. *ACS Appl. Mater. Interfaces* **2016**, *8*, 33197–33209. [CrossRef]

45. Casey, L.S.; Wilson, L.D. Investigation of Chitosan-PVA Composite Films and Their Adsorption Properties. *J. Geosci. Environ. Prot.* **2015**, *3*, 78–84. [CrossRef]
46. Dolatkhah, A. Investigation of Stimuli-Responsive Polymer Nanocomposites for Dye Treatment in Aqueous Solution. Ph.D. Thesis, University of Saskatchewan, Saskatoon, SK, Canada, 2019.
47. Sharma, V.; Rekha, P.; Mohanty, P. Nanoporous Hypercrosslinked Polyaniline: An Efficient Adsorbent for the Adsorptive Removal of Cationic and Anionic Dyes. *J. Mol. Liq.* **2016**, *222*, 1091–1100. [CrossRef]
48. Shen, J.; Shahid, S.; Amura, I.; Sarihan, A.; Tian, M.; Emanuelsson, E.A. Enhanced adsorption of cationic and anionic dyes from aqueous solutions by polyacid doped polyaniline. *Synth. Met.* **2018**, *245*, 151–159. [CrossRef]
49. Kajjumba, G.W.; Emik, S.; Öngen, A.; Özcan, H.K.; Aydın, S. Modelling of Adsorption Kinetic Processes—Errors, Theory and Application. In *Advanced Sorption Process Applications*; IntechOpen: London, UK, 2018. [CrossRef]
50. MacDiarmid, A.G. *The Polyanilines: A Novel Class of Conducting Polymers*; University of Pennsylvania: Philadelphia, PA, USA, 1992.
51. MacDiarmid, A.G.; Epstein, A.J. Polyanilines: A Novel Class of Conducting Polymers. *Faraday Discuss. Chem. Soc.* **1989**, *88*, 317–332. [CrossRef]
52. Wypych, G. *Handbook of Fillers*, 4th ed.; ChemTec Publishing: Toronto, ON, Canada, 2016; pp. 359–360.
53. Udoetok, I.A.; Wilson, L.D.; Headley, J.V. "Pillaring Effects" in Cross-Linked Cellulose Biopolymers: A Study of Structure and Properties. *Int. J. Polym. Sci.* **2018**, *2018*, 1–13. [CrossRef]